Programming tunable active dynamics in a self-propelled robot

Somnath Paramanick¹, Arnab Pal², Harsh Soni³, and Nitin Kumar^{1*}

¹Department of Physics,

Indian Institute of Technology Bombay Powai,

Mumbai 400076, India

² The Institute of Mathematical Sciences,

CIT Campus, Taramani, Chennai 600113,

India & Homi Bhabha National Institute,

Training School Complex,

Anushakti Nagar, Mumbai 400094, India

³ School of Physical Sciences,

Indian Institute of Technology Mandi, Mandi 175001, India

(Dated: November 7, 2023)

We present a scheme for producing tunable active dynamics in a self-propelled robotic device. The robot moves using the differential drive mechanism where two wheels can vary their instantaneous velocities independently. These velocities are calculated by equating robot's equations of motion in two dimensions with well-established active particle models and encoded into the robot's microcontroller. We demonstrate that the robot can depict active Brownian, run and tumble, and Brownian dynamics with a wide range of parameters. The resulting motion analyzed using particle tracking shows excellent agreement with the theoretically predicted trajectories. Finally, we demonstrate that its motion can be switched between different dynamics using light intensity as an external parameter. This work opens an avenue for designing tunable active systems with the potential of revealing the physics of active matter and its application for bio- and nature-inspired robotics.

I. INTRODUCTION

Active matter refers to systems comprised of selfpropelled particles that consume energy to perform mechanical work [1–4]. Such systems exhibit striking nonequilibrium phenomena such as collective dynamics, selforganization, and anomalous mechanical properties ubiquitous in the natural and biological world [5–17]. Over the past few decades, numerous analytical, numerical, and experimental studies have advanced our understanding of such systems. Yet we are just beginning to realize the potential of active matter in building smart, adaptable materials and autonomous devices [18–20]. Achieving this will require better control over individual particle dynamics and inter-particle interactions. Thus, many studies in recent years have reported concerted efforts to achieve programmable control on active matter spanning a broad range of length scales [21–32]. Here, we develop a novel active matter system consisting of a collection of smart programmable self-propelled robots capable of sensing their environment using onboard sensors. As a first step, in this paper, we present simple protocols for extracting tunable active dynamics in a single robot.

Previous studies have shown that emerging properties in active systems depend on the self-propulsion mechanism of individual agents, the strength of alignment interaction, and the nature of the surrounding medium [2]. Therefore, an artificial active material must incorporate all these features to replicate complex nonequilibrium properties displayed by active systems. Yet, broadly speaking, modeling individual constituent dynamics using simple theoretical frameworks of active Brownian particles (ABP) and run-and-tumble particles (RTP) has proven successful in replicating emerging phenomena with great success [3]. Thus, a robotic device, due to its programmability, becomes a natural choice to mimic controlled active particle dynamics. While there are many examples in the literature where robots perform programmable complex self-assembly [33] as well as spontaneous collective behavior [34–37] they rely on vibration motors for locomotion [33–35]. More recently, differential drive robots have also been reported which show much better control of individual dynamics [26, 38–40]. Yet, a detailed protocol to program them with well-established theoretical models of ABP, RTP, and Brownian particle (BP) is missing.

In this work, we present a robotic system that displays a variety of active dynamics with many controllable parameters. Our robot is circularly shaped and propels itself using the differential drive mechanism. In addition, the robot also houses hardware components like multiple infrared (IR) and light intensity (LI) sensors which help it detect environmental factors like obstacles and ambient light. We demonstrate that with its two wheels oppositely placed at a diameter distance away, its center of mass can display a variety of motions depending entirely on the instantaneous wheel velocities. In particular, we show our results on the following three models: (i) Active Brownian particle (ABP) with and without translational noise, (ii) Run and Tumble particle (RTP), and (iii) Brownian particle (BP) dynamics. These results are found to be in excellent agreement with our theoret-

^{*} nkumar@iitb.ac.in

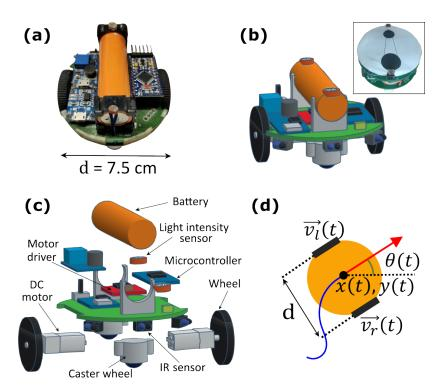


FIG. 1. Robot model: (a) The robot used in the experiment with its diameter indicated. (b) A schematic representation of the same robot. The inset shows the top view of the robot covered with a white cap with two black circles on top along its orientation. (c) An expanded view highlighting its important hardware components. (d) Robot's position (x(t), y(t)) and orientation $\theta(t)$ vary as a function of the instantaneous left and right wheel's velocities $(v_l(t))$ and $v_r(t)$, respectively), resulting in the centre of mass tracing out a trajectory indicated by the blue solid line.

ical modeling. We also show that the robot can be programmed to switch between these dynamics as a function of the ambient light intensity, providing spatiotemporal control over its motion. Taken together, our results propose a novel experimental system based on smart programmable robots that provide an ideal platform for exploring problems related to active and living systems with potential in future material design.

II. ROBOT MODEL

Our robot is a circularly shaped electronic gadget with a diameter of 7.5 cm and a height of 5 cm (See Fig. 1(a-c)). It is assembled using various hardware components as indicated in Fig. 1(c). It has two rubber wheels of diameter 3.3 cm placed at the two ends of Two caster wheels are placed in the its diameter. perpendicular direction for support. It also carries six IR sensors symmetrically placed along the circumference to detect obstacles. Two light intensity (LI) sensors, each placed at the front and back, enable the robot to detect the ambient light intensity gradients. We use the differential drive technique for the robot's movement on a 2D plane surface by controlling the velocity of the wheels independently [41]. The programs, written using Arduino IDE software, are loaded onto an Arduino pro

mini microcontroller board (3.3 V, 8 MHz version), and the output signal is fed to the motor driver (Dual TB6612FNG by SparkFun), that rotates the wheels using two separate DC motors. The signal from the microcontroller provides 256 different analog voltage levels from zero to maximum voltage (5V) to the motors. This gives each wheel a range of velocities maximum of up to 27 cm/sec. All these components are powered using a Li-ion battery. A brief summary of robot functioning is presented in SI Fig.1. The robot performs its dynamics on a flat surface of dimensions 90 cm \times 120 cm with a white background. We use an overhead projector connected to a computer to illuminate the surface with the desired light intensity. We capture the dynamics of the robot using a high-speed camera from the top and perform image analysis to extract instantaneous position and orientation (See Appendix A).

We begin by writing the equations of motion of the robot in two dimensions. Let $v_l(t)$ and $v_r(t)$ be the velocities of the left and right wheels of the robot along its orientation at time t (See Fig. 1(d)). Then, the equations of motion for the position (x(t), y(t)) and the orientation

angle $\theta(t)$ of the robot read

$$\dot{x}(t) = \frac{v_l(t) + v_r(t)}{2} \cos \theta(t),$$

$$\dot{y}(t) = \frac{v_l(t) + v_r(t)}{2} \sin \theta(t),$$

$$\dot{\theta}(t) = \frac{v_r(t) - v_l(t)}{d},$$
(1)

where d is the diameter of the robot, and the dot stands for the time derivative. We next show that purely based on the instantaneous values of v_l and v_r , we can program the robot to perform desired stochastic dynamics. $\frac{1}{24}$

III. RESULTS AND DISCUSSION

A. ABP model without translational noise

A distinctive feature of a polar active particle is its finite self-propulsion speed. In general, it can have rotational as well as translational noise. We first study the case without an explicit source of translational noise. In that case, it is often modeled as an ABP, which is equivalent to a biased random walk in two dimensions where the particle always moves in the direction of its instantaneous orientation. Consequently, the ABP moves with a constant speed but its direction changes randomly in the plane. The dynamics of an ABP of speed v is governed by the following equations of motion:

$$\dot{x}(t) = v \cos \theta(t),
\dot{y}(t) = v \sin \theta(t),
\dot{\theta}(t) = \zeta(t).$$
(2)

where ζ is the instantaneous rotational speed of the ABP; it is a white noise with a zero mean and is often modeled as white Gaussian noise. Here, we construct an active Brownian robot with ζ having a uniform distribution between $[-\eta, \eta]$. In order to produce an ABP motion of given η and v in our robot, we compare (2) and (1) to obtain the expressions of v_l and v_r , which yields

$$v_l(t) = \frac{2v + \zeta(t)d}{2},$$

$$v_r(t) = \frac{2v - \zeta(t)d}{2}.$$
(3)

The values of v_l and v_r are updated in the robot after every ϵ seconds, termed as delay time. In experiments, the accessible values of parameters η and ϵ lie between 1 - 6 rad/s and 0.1 - 0.9 s, respectively.

When implemented in the robot, it mimics the ABP motion quite well. A typical trajectory of the robot is shown in Fig. 2(a) and SI movie S1. To get this unbounded free particle trajectory, we use boundary wall detection using IR sensors to remove the confinement effects (See Appendix B). The zoomed-in part of the

trajectory ascertains the absence of translational noise at short time scales. The mean squared displacement (MSD) shows a transition from ballistic to diffusive behavior, a hallmark feature of the ABP dynamics (see Fig. 2(b)). Using a simple theoretical calculation, we obtain the following expression for the MSD [42, 43]

$$\langle \Delta r^2(\tau) \rangle = \frac{2v^2}{D_r} [\tau + \frac{1}{D_r} (e^{-D_r \tau} - 1)],$$
 (4)

where $D_r = \epsilon \langle \zeta^2 \rangle / 2 = \epsilon \eta^2 / 6$ (see Appendix C). The solid red line in Fig. 2(b) represents analytically obtained MSD, which shows an excellent agreement with our experimental data. We further plot angular MSD defined as $\langle \Delta \theta^2(\tau) \rangle$ for varying ϵ and η independently (See Figs. 2(c) and 2(d)). Interestingly, we find that it scales linearly with τ only for $\tau > \epsilon$, whereas for $\tau < \epsilon$, the plot is ballistic with τ^2 scaling. This happens because during the time duration ϵ , the robot always rotates with a constant angular velocity of magnitude $|(v_l - v_r)/d|$, resulting in $\Delta\theta$ scaling linearly with τ . For given ϵ and η , the experimental value of D_r is measured by line-fitting $\langle \Delta \theta^2(\tau) \rangle$, using the formula $\langle \Delta \theta^2(\tau) \rangle = 2D_r \tau$. We then plot D_r as a function of ϵ and η in the insets of Figs. 2(c) and 2(d), respectively, showing D_r indeed scaling according to the expression $D_r = \epsilon \eta^2/6$, as predicted by

We also measure spatial velocity autocorrelation function, $C(l) = \langle \mathbf{v}(r).\mathbf{v}(r+l) \rangle_r / \mathbf{v}^2$, where r is the distance traveled by the robot, with respect to l for different values of η keeping ϵ constant at 0.25 s as shown in Fig. 2(e) inset. We find that $C(l) \propto e^{-l/L_s}$, where L_s is the persistence length. Using the above relation, we extracted L_s for different η . We find that L_s decreases algebraically with η with an exponent of "-2". This also agrees with the theory since $L_s = v/D_r \propto \eta^{-2}$.

B. ABP model with translational noise

In general, at small time scales, a polar particle may have translational noise along as well as normal to its orientation. In this case, therefore, v in (2) is not a constant and rather fluctuates around its mean value. We achieve this by generating $v_l(t)$ and $v_r(t)$ from two statistically independent random uniform distributions in a range of 2V with a finite mean v_a , i.e., in the interval $[v_a - V, v_a + V]$. Here V quantifies the strength of the translational noise. Interestingly, since our robot, at any instance, can only move along the direction of its wheels, this noise features only in the velocity component, which is parallel to its orientation, while noise normal to its orientation is forbidden. As a result, both $\dot{\theta}(t)$ and v(t) become random variables with zero and a non-zero mean $(=v_a)$, respectively.

Fig. 3(a) and SI movie S2 show a typical trajectory of the robot following noisy ABP dynamics. At long time scales, the trajectory qualitatively looks similar to the ABP without translational noise (Fig. 2(b)) but differs

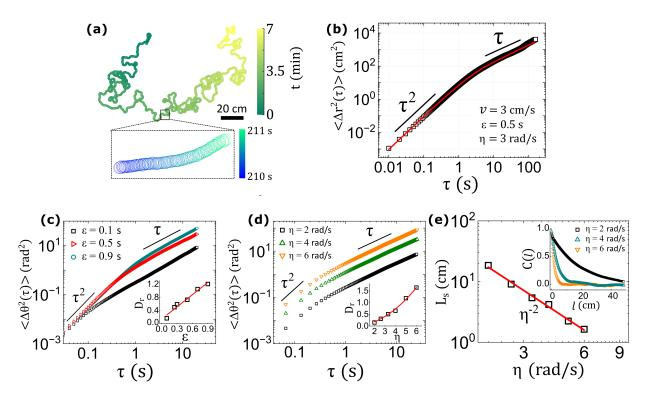


FIG. 2. **ABP model without translational noise**: (a) A typical trajectory of the robot following ABP dynamics with velocity v=3 cm/s, delay time $\epsilon=0.5$ s, and rotational noise $\eta=3$ rad/s. The color bar represents the time. The zoomedin portion of the trajectory shows the robot moving with a constant velocity at all time steps, indicative of the absence of translational noise at short time scales. (b) Translational mean-square displacement (MSD) of the trajectory plotted as a function of time τ showing a ballistic ($\sim \tau^2$) to diffusive ($\sim \tau$) transition. The solid line shows the fit with the analytical expression given by (4). (c) Angular MSD, $<\Delta\theta^2(\tau)>$, plotted for three values of ϵ keeping $\eta=3$ rad/s. $<\Delta\theta^2(\tau)>$ also undergoes a ballistic to diffusive transition at time ϵ . (Inset) The experimental values of D_r , measured by line fitting the linear part of the MSD, show linear scaling with ϵ . (d) Angular MSD as a function of τ for different values of η keeping ϵ fixed at 0.25 s. (Inset) D_r extracted from the plots increases quadratically with η . (e) Persistence length L_s shows an algebraic decay with η with an exponent consistent with theory. L_s is extracted by fitting an exponential function to the spatial velocity autocorrelation function, $C(l) = \langle \mathbf{v}(r).\mathbf{v}(r+l)\rangle_r/\mathbf{v}^2$ shown in the inset.

significantly at short time scales as depicted by frequent back-and-forth events in the zoomed-in trajectory. We plot experimentally measured MSD in Fig. 3(b), which shows scaling with τ at both short and very long time scales as reported in past studies [43]. We solve the Langevin equation for this case and obtain the following expression of the MSD

$$\langle \Delta r^2(\tau) \rangle = 4D_t \tau + \frac{2v_a^2}{D_r^2} [D_r \tau + (e^{-D_r \tau} - 1)],$$
 (5)

where $D_t = \epsilon V^2/24$ and $D_r = \epsilon V^2/3d^2$ are the translational and the rotational diffusion constants, respectively (see Appendix C). Again the experimental data agree well with the analytical MSD expression (solid red line) over the entire range of time scales (Fig. 3(b)). Clearly, in the limits $\tau \to 0$ and $\tau \to \infty$, (5) reduces to $\langle \Delta r^2(\tau) \rangle_{\tau \to 0} = 4D_t \tau$ and $\langle \Delta r^2(\tau) \rangle_{\tau \to \infty} = 4[D_t + v_a^2/(2D_r)]\tau$, respectively, showing an agreement with our experimental results.

C. Brownian particle model

A Brownian particle (BP) in two dimensions can move in any direction with an equal probability. However, quite obviously, the wheels of our robot can move only along its direction of orientation, not normal to it. Here we show that it is possible for our robot to perform BP dynamics with limited movement of its wheels. Notably, the ABP motion with noise described in the previous section reduces to the BP dynamics when $v_a = 0$. As a result, both v(t) and $\dot{\theta}$ become random variables with zero mean. Fig. 3(c) and SI movie S3 show the trajectory of the robot following the BP model with V = 7 cm/s and $\epsilon = 0.2$ s. The resulting MSD shows that at short times ($<\epsilon$) the motion is ballistic, and at longer times it is diffusive (see Fig. 3(d)), similar to $\langle \Delta \theta^2(\tau) \rangle$ observed in Figs. 2(c) and 2(d). Again, the ballistic regime is a consequence of finite velocity events experienced by both left and right wheels over a time interval of ϵ . This is further verified by the fact that the crossover from ballistic to diffusive regime happens exactly after ϵ .

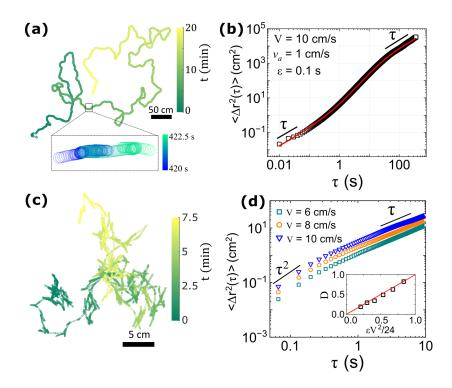


FIG. 3. **ABP model with translational noise and BP model**: (a) Typical trajectory of the robot programmed to follow ABP model with translational noise having V=10 cm/s, $\epsilon=0.1$ s, and $v_a=1$ cm/s. The color bar represents the time. The zoomed-in trajectory shows the presence of translational noise in the form of significant back-and-forth events along the robot's orientation. (b) The translational MSD shows a diffusive to super-diffusive to diffusive transition as a function of time. The solid line is fit with the analytical expression given by (5). (c) A typical trajectory of the robot following a BP motion with V=7 cm/s, $\epsilon=0.2$ s, and $v_a=0$ cm/s. The color bar represents the time of motion. (d) The translational MSD of the BP motion plotted for three values of V keeping ϵ fixed at 0.2 s shows a ballistic to diffusive transition. The ballistic motion is a consequence of the finite delay time ϵ which also sets the crossover time for all the curves. The inset shows the diffusion constant D measured from the MSD curves matches with $\epsilon V^2/24$ as predicted by the theory.

Moreover, since $\langle \Delta r^2(\tau) \rangle = 4D\tau$, we extract the diffusion constants D from the MSD plots for various values of V and ϵ . We plot this value with the analytical result, which predicts $D = \epsilon \langle v^2 \rangle / 4 = \epsilon V^2 / 24$ in Fig. 3(d) inset. Clearly, we find an excellent agreement with the theory (solid line indicating the equality).

D. Run and tumble particle model

We now turn our attention to the RTP models, where an individual particle moves in a straight line interrupted by frequent tumble events that randomize its run direction (Fig. 4(a)) [44, 45]. Such motion is widely observed in micro-organisms like bacteria [46] and even in active granular particles [47]. In the case of our robot, it runs when the left and right wheels have the same velocities, i.e., $v_l = v_r = v_{\rm run}$, and it tumbles to a new direction when $v_l = -v_r$. A typical trajectory of the robot performing RTP motion is shown in Fig. 4(b) and SI movie S4 with its instantaneous speed plotted in Fig. 4(c). Here, the robot runs with a constant speed $v_{\rm run}$ for a duration τ_r (run time), after which it tumbles over a time τ_t (tumble duration). It is important to highlight that

 τ_t can never be zero in our experiments since the robot can never tumble instantaneously. Inspired by the experimental observations in bacteria [46], we choose τ_r from an exponential distribution $P(\tau_r) = \gamma e^{-\gamma \tau_r}$, whereas τ_t is kept constant for all tumble events. This is achieved by scaling the tumble speed with the tumble angle, which is chosen randomly between 0 to 360 degrees. The RTP trajectory shown in Fig. 4(b) has $v_{\rm run} = 5$ cm/s, $\gamma = 3$ s^{-1} , and $\tau_t = 0.5$ s. Later, we perform experiments for various τ_r distributions characterized by γ at fixed τ_t 0.5 s. The resulting MSD is shown in Fig. 4(d), showing a ballistic ($\sim \tau^2$) to diffusive ($\sim \tau$) transition with transition time decreasing as we increase γ . However, when we vary τ_t while keeping γ constant (Fig. 4(e) for γ = 1 s⁻¹), the transition time remains independent of τ_t . Regardless, the MSD measured experimentally shows an excellent agreement with the theoretical expression given by [48]

$$\langle \Delta r^2(\tau) \rangle = \frac{1}{1 + \gamma \tau_t} \frac{2v_{\text{run}}^2}{\gamma^2} (\gamma \tau - 1 + e^{-\gamma \tau}).$$
 (6)

The solid red lines in Fig. 4(d) and (e) show the fit, which is in excellent agreement with the experimental results.

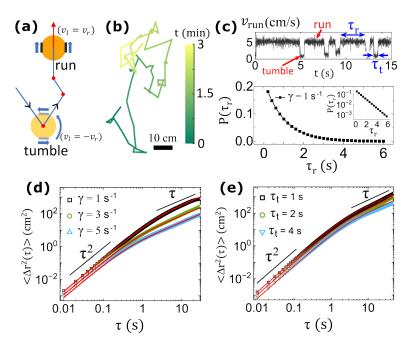


FIG. 4. **RTP model**: (a) A typical schematic of the robot mimicking RTP model. A run event is characterized by a straight trajectory when $v_l = v_r$. The robot tumbles while $v_l = -v_r$ and finds a new run direction randomly. (b) The trajectory of the robot for a duration of 3 minutes, programmed to follow RTP model. The color bar shows the time. (c) The top plot shows the instantaneous speed of the robot, which switches between $v_{\text{run}} = 5$ cm/s and $v_{\text{run}} = 0$, representing run and tumble, respectively. τ_r and τ_t represent run and tumble duration, respectively. τ_t is constant during the motion, whereas τ_r is extracted from an exponential distribution $P(\tau_r) = \gamma e^{-\gamma \tau_r}$ as shown in the bottom plot. A linear semi-log plot in the inset verifies the exponential distribution. Parameter values for the trajectory shown in (b) are $v_{\text{run}} = 5$ cm/s, $\gamma = 3$ s⁻¹, and $\tau_t = 0.5$ s. (d) Translational MSD as a function of time for three different γ values keeping $\tau_t = 0.5$ s. Solid pink lines are the fit with the theoretical expression given by (6). (e) Translational MSD for three different τ_t values keeping the τ_r distribution fixed with $\gamma = 1$ s⁻¹. Again, solid lines represent the fit with the same theoretical expression.

E. Light-activated dynamics

Finally, we demonstrate that the robot can be programmed to switch between the various dynamics discussed above using light intensity as an external parameter. Since our robot is equipped with two LI sensors at its front and back (Fig. 1(a) & (b), it continuously measures the value of ambient light intensity, which is set using the overhead projector. We load multiple programs onto the robot's microcontroller and assign light intensity values for each program. For example, we can program the robot to display ABP dynamics when the measured light intensity is between $I_1 - I_2$, BP between $I_3 - I_4$, etc., where I_1 , I_2 , I_3 &, I_4 are arbitrary. We summarize this result in SI movie S5, where a robot is programmed to display BP, ABP, and RTP motion as a function of increasing light intensity.

IV. CONCLUSION

Here, we introduced a novel experimental system consisting of self-propelled robots. The robots are smart computing devices capable of executing a preloaded program and simulating it to in-plane dynamics with ex-

cellent control. Using hardware components like IR and LI sensors, they can also detect obstacles and ambient light intensity and modify their motion as required. The robots are driven by two wheels placed diametrically opposite to each other and move independently with velocities v_l and v_r , respectively. We first show that instantaneous values of v_l and v_r calculated from scalar active particle models like Active Brownian, Run and Tumble, and Brownian motion reproduce desired stochastic dynamics in the centre of mass of the robots quite accurately. The experimental parameter space over which this motion can be tuned is quite exhaustive and highly tunable. We also demonstrated the control over robot motion using ambient light as an external control parameter.

Overall, the experimental system presented in this paper holds great potential in unraveling laws governing the non-equilibrium physics of active and living systems with applications to smart and adaptive material design. In a nutshell, our robots are a simple assembly of electronic and mechanical elements, and we coupled the well-developed theoretical ideas of scalar active particles with the mechanics of such a differential-driven robot. To the best of our knowledge, this is the first-ever study in this direction and carries vast importance considering the rise

of the use of programmable particles in active and living matter experiments. The next step is to use a collection of such robots, which offers a significant advantage over already existing experimental systems due to our ability to control individual dynamics with great control. Moreover, we can also engender complex inter-robot interaction using IR and LI sensors which can test not only existing theories in the field but also generate novel dynamical phases hitherto unknown. Furthermore, a collection of such robots also offers possible applications for bio-inspired and nature-inspired robotics.

ACKNOWLEDGEMENTS

NK acknowledges financial support from DST-SERB for CRG grant number CRG/2020/002925 and IITB for the seed grant. NK also thanks Sriram Ramaswamy and Sanjib Shabhapandit for productive discussions. AP acknowledges research support from the DST-SERB Start-up Research Grant Number SRG/2022/000080 and the Department of Atomic Energy, India. HS acknowledges SERB for the SRG (grant no. SRG/2022/000061-G). SP thanks CSIR India for research fellowship.

APPENDIX A: Image-analysis technique

In experiments on modeling the robot dynamics, we cover the robot's components (except the light intensity sensors) with a white cap with two black circles drawn on top of it, one bigger than the other, along the robot's orientation. We then use MATLAB's blob analysis to extract their position coordinates. The vector connecting them provides the instantaneous orientation of the robot, and the midpoint of the line connecting them provides the center-of-mass coordinate. The frame rate at which movies are captured varies between 10-100 depending on the robot's speed. The movies are captured for a duration of 1 hour for each model.

APPENDIX B: Removing confinement effect

Theoretical models of ABP, RTP, and BP dynamics consider an unbounded motion of the particle. In our experiments, we use the following protocol to remove confinement effects caused by boundary walls. Once the robot detects the boundary through its IR sensors, it moves 40 cm in the reverse direction while maintaining its orientation. Later, we remove these straight trajectories from the experiments and stitch all the stochastic tracks together by shifting the coordinates appropriately (See Fig.2 in SI). This creates a continuous free particle motion that is effectively unconfined.

APPENDIX C: Theoretical calculation

1. ABP model without translational noise

In general, the equations of motion for the robot are given by

$$\dot{x}(t) = v(t)\cos\theta(t), \tag{7a}$$

$$\dot{y}(t) = v(t)\sin\theta(t), \tag{7b}$$

$$\dot{\theta}(t) = \zeta(t), \tag{7c}$$

where v(t) is the component of the instantaneous robot velocity along its orientation $\mathbf{n} = (\cos \theta(t), \sin \theta(t))$. The values of v and ζ are varied discretely with the step size of ϵ second. For mimicking the ABP model, v is kept constant and $\zeta(t)$ is chosen to be a random number with a uniform distribution between $[-\eta, \eta]$. For the time scales much larger than ϵ ,

$$\langle \zeta(t)\zeta(t')\rangle = 2D_r\delta(t-t'),$$
 (8)

where D_r is the rotational diffusion constant. It is straightforward to show that [49]

$$\left\langle \left[\theta(\tau) - \theta(0)\right]^2 \right\rangle = 2D_r \tau.$$
 (9)

Here the angular bracket represents the ensemble average. Whereas, from the discrete form of (7c),

$$\theta(\tau) = \theta(0) + \epsilon \sum_{i=1}^{N_{\tau}} \zeta_i, \tag{10}$$

where $\zeta_i \equiv \zeta(i\epsilon)$ and $N_\tau = \tau/\epsilon$. As the random number ζ_i has the uniform probability distribution between $[-\eta, \eta]$,

$$\langle \zeta_i \zeta_j \rangle = \delta_{ij} \frac{\eta^2}{3}. \tag{11}$$

Then, from (10),

$$\left\langle \left[\theta(\tau) - \theta(0)\right]^{2} \right\rangle = \epsilon^{2} \sum_{i=1}^{N_{\tau}} \sum_{j=1}^{N_{\tau}} \left\langle \zeta_{i} \zeta_{j} \right\rangle$$

$$= \epsilon^{2} \sum_{i=1}^{N_{\tau}} \left\langle \zeta_{i}^{2} \right\rangle$$

$$= \epsilon^{2} N_{\tau} \frac{\eta^{2}}{3}$$

$$= \epsilon \tau \frac{\eta^{2}}{3}$$
(12)

Comparing the above equation with (9), we obtain

$$D_r = \epsilon \frac{\eta^2}{6}.\tag{13}$$

2. ABP with translational noise

In this case, v(t) in (7) is not constant, it rather fluctuates around its mean value. The values of v(t) and $\zeta(t)$ in terms of the velocities of the left and right wheels of the robot, v_l and v_r , are given by

$$v(t) = \frac{v_r(t) + v_l(t)}{2},$$
 (14a)

$$\zeta(t) = \frac{v_r(t) - v_l(t)}{d}, \tag{14b}$$

where d is the diameter of the robot. Here v_l and v_r are statistically independent random numbers with a uniform probability distribution in the range $[v_a - V, v_a + V]$. Then, one can readily show that

$$\langle v_r(i\epsilon)v_r(j\epsilon)\rangle = \delta_{ij}\frac{V^2}{3} + v_a^2,$$
 (15)

$$\langle v_l(i\epsilon)v_l(i\epsilon)\rangle = \delta_{ij}\frac{V^2}{3} + v_a^2,$$
 (16)

$$\langle v_r(i\epsilon)v_l(j\epsilon)\rangle = 0.$$
 (17)

Then the relations (14) give

$$\langle v(i\epsilon)v(j\epsilon)\rangle = \delta_{ij}\frac{V^2}{6} + v_a^2,$$
 (18)

$$\langle \zeta(i\epsilon)\zeta(j\epsilon)\rangle = \delta_{ij}\frac{2V^2}{3d^2},$$
 (19)

$$\langle v(i\epsilon)\zeta(j\epsilon)\rangle = 0.$$
 (20)

For the time scales much larger than ϵ , it is obvious from (18) that

$$\langle v(t)v(t')\rangle = 4D_t\delta(t-t') + v_a^2,\tag{21}$$

and ζ follows the correlation relation given by (8). Following the similar steps as done in Sec IV 1, one can show that

$$D_r = \frac{\epsilon V^2}{3d^2},\tag{22}$$

$$D_t = \frac{\epsilon V^2}{24}. (23)$$

The mean square displacement can then be calculated as follows

$$\Delta r^{2}(\tau) = \langle [\mathbf{r}(\tau) - \mathbf{r}(0)] \cdot [\mathbf{r}(\tau) - \mathbf{r}(0)] \rangle$$

$$= \left\langle \int_{0}^{\tau} dt \int_{0}^{\tau} dt' v(t) v(t') \cos [\theta(t) - \theta(t')] \right\rangle$$

$$= \int_{0}^{\tau} dt \int_{0}^{\tau} dt' \langle v(t) v(t') \cos [\theta(t) - \theta(t')] \rangle (24)$$

As v and ζ are statistically independent of each other [from (20)], we have

$$\Delta r^{2}(\tau) = \int_{0}^{\tau} dt \int_{0}^{\tau} dt' \langle v(t)v(t')\rangle \langle \cos [\theta(t) - \theta(t')] \rangle.$$

Using (21) and the following relation [42, 50–52]

$$\langle \cos \left[\theta(t) - \theta(t') \right] \rangle = \exp \left(-D_r \left| t - t' \right| \right),$$
 (25)

we arrive at

$$\Delta r^{2}(\tau) = \int_{0}^{\tau} dt \int_{0}^{\tau} dt' \Big\{ \left[4D_{t}\delta(t - t') + v_{a}^{2} \right] \times \exp\left(-D_{r} |t - t'|\right) \Big\}$$
$$= 4D_{t}\tau + \frac{2v_{a}^{2}}{D_{r}^{2}} \left[D_{r}\tau + \left(e^{-D_{r}\tau} - 1\right) \right], (26)$$

which was used in Eq. (5). To imitate the BP model, we set $v_a=0$ to obtain

$$\Delta r^2(\tau) = 4D_t \tau. (27)$$

Note that here the dynamics of the robot does not depend on the rotational diffusion constant D_r .

- S. Ramaswamy, The mechanics and statistics of active matter, Annu. Rev. Condens. Matter Phys. 1, 323 (2010).
- [2] M. C. Marchetti, J.-F. Joanny, S. Ramaswamy, T. B. Liverpool, J. Prost, M. Rao, and R. A. Simha, Hydrodynamics of soft active matter, Reviews of modern physics 85, 1143 (2013).
- [3] H. Chaté, Dry aligning dilute active matter, Annual Review of Condensed Matter Physics 11, 189 (2020).
- [4] J. Toner, Y. Tu, and S. Ramaswamy, Hydrodynamics and phases of flocks, Annals of Physics 318, 170 (2005).
- [5] N. Kumar, H. Soni, S. Ramaswamy, and A. Sood, Flocking at a distance in active granular matter, Nature communications 5, 4688 (2014).
- [6] T. Sanchez, D. T. Chen, S. J. DeCamp, M. Heymann, and Z. Dogic, Spontaneous motion in hierarchically assembled active matter, Nature 491, 431 (2012).
- [7] J. Brugués and D. Needleman, Physical basis of spindle self-organization, Proceedings of the National Academy of Sciences 111, 18496 (2014).
- [8] M. E. Cates and J. Tailleur, Motility-induced phase separation, Annu. Rev. Condens. Matter Phys. 6, 219 (2015).
- [9] N. Kumar, R. Zhang, S. A. Redford, J. J. de Pablo, and M. L. Gardel, Catapulting of topological defects through elasticity bands in active nematics, Soft Matter 18, 5271 (2022).
- [10] J. Palacci, S. Sacanna, A. P. Steinberg, D. J. Pine, and P. M. Chaikin, Living crystals of light-activated colloidal surfers, Science 339, 936 (2013).
- [11] N. Kumar, R. Zhang, J. J. De Pablo, and M. L. Gardel, Tunable structure and dynamics of active liquid crystals, Science advances 4, eaat7779 (2018).
- [12] R. A. Simha and S. Ramaswamy, Hydrodynamic fluctuations and instabilities in ordered suspensions of self-propelled particles, Physical review letters 89, 058101 (2002).
- [13] Y. Hatwalne, S. Ramaswamy, M. Rao, and R. A. Simha, Rheology of active-particle suspensions, Physical review letters 92, 118101 (2004).
- [14] S. Rafaï, L. Jibuti, and P. Peyla, Effective viscosity of microswimmer suspensions, Physical Review Letters 104, 098102 (2010).
- [15] H. M. López, J. Gachelin, C. Douarche, H. Auradou, and E. Clément, Turning bacteria suspensions into superfluids, Physical review letters 115, 028301 (2015).
- [16] M. Fruchart, C. Scheibner, and V. Vitelli, Odd viscosity and odd elasticity, Annual Review of Condensed Matter Physics 14, 471 (2023).
- [17] L. M. Nash, D. Kleckner, A. Read, V. Vitelli, A. M. Turner, and W. T. Irvine, Topological mechanics of gyroscopic metamaterials, Proceedings of the National Academy of Sciences 112, 14495 (2015).
- [18] M. Brandenbourger, X. Locsin, E. Lerner, and C. Coulais, Non-reciprocal robotic metamaterials, Nature communications 10, 4608 (2019).
- [19] A. Souslov, B. C. Van Zuiden, D. Bartolo, and V. Vitelli, Topological sound in active-liquid metamaterials, Nature Physics 13, 1091 (2017).
- [20] G. R. Gossweiler, C. L. Brown, G. B. Hewage, E. Sapiro-Gheiler, W. J. Trautman, G. W. Welshofer, and S. L. Craig, Mechanochemically active soft robots, ACS applied materials & interfaces 7, 22431 (2015).

- [21] A. Unruh, A. M. Brooks, I. S. Aranson, and A. Sen, Programming motion of platinum microparticles: From linear to orbital, ACS Applied Engineering Materials (2023).
- [22] R. Zhang, S. A. Redford, P. V.Ruijgrok, N. Kumar, A. Mozaffari, S. Zemsky, A. R. Dinner, V. Vitelli, Z. Bryant, M. L. Gardel, and J. J. de Pablo, Spatiotemporal control of liquid crystal structure and dynamics through activity patterning, Nature Materials 20, 875 (2021).
- [23] I. Buttinoni, G. Volpe, F. Kümmel, G. Volpe, and C. Bechinger, Active brownian motion tunable by light, Journal of Physics: Condensed Matter 24, 284129 (2012).
- [24] S. Li, R. Batra, D. Brown, H.-D. Chang, N. Ranganathan, C. Hoberman, D. Rus, and H. Lipson, Particle robotics based on statistical mechanics of loosely coupled components, Nature 567, 361 (2019).
- [25] M. A. Fernandez-Rodriguez, F. Grillo, L. Alvarez, M. Rathlef, I. Buttinoni, G. Volpe, and L. Isa, Feedbackcontrolled active brownian colloids with space-dependent rotational dynamics, Nature communications 11, 4223 (2020).
- [26] S. G. Prasath, S. Mandal, F. Giardina, J. Kennedy, V. N. Murthy, and L. Mahadevan, Dynamics of cooperative excavation in ant and robot collectives, Elife 11, e79638 (2022).
- [27] F. Siebers, A. Jayaram, P. Blümler, and T. Speck, Exploiting compositional disorder in collectives of light-driven circle walkers, Science Advances 9, eadf5443 (2023).
- [28] B. Nakayama, H. Nagase, H. Takahashi, Y. Saito, S. Hatayama, K. Makino, E. Yamamoto, and T. Saiki, Tunable pheromone interactions among microswimmers, Proceedings of the National Academy of Sciences 120, e2213713120 (2023).
- [29] N. Aubert-Kato, C. Fosseprez, G. Gines, I. Kawamata, H. Dinh, L. Cazenille, A. Estevez-Tores, M. Hagiya, Y. Rondelez, and N. Bredeche, Evolutionary optimization of self-assembly in a swarm of bio-micro-robots, in Proceedings of the Genetic and Evolutionary Computation Conference (2017) pp. 59–66.
- [30] Z. Zeravcic, V. N. Manoharan, and M. P. Brenner, Colloquium: Toward living matter with colloidal particles, Reviews of Modern Physics 89, 031001 (2017).
- [31] R. Zhang, S. A. Redford, P. V. Ruijgrok, N. Kumar, A. Mozaffari, S. Zemsky, A. R. Dinner, V. Vitelli, Z. Bryant, M. L. Gardel, et al., Spatiotemporal control of liquid crystal structure and dynamics through activity patterning, Nature materials 20, 875 (2021).
- [32] L. M. Lemma, M. Varghese, T. D. Ross, M. Thomson, A. Baskaran, and Z. Dogic, Spatiotemporal patterning of extensile active stresses in microtubule-based active fluids, arXiv preprint arXiv:2209.06277 (2022).
- [33] M. Rubenstein, A. Cornejo, and R. Nagpal, Programmable self-assembly in a thousand-robot swarm, Science **345**, 795 (2014).
- [34] A. Deblais, T. Barois, T. Guerin, P.-H. Delville, R. Vaudaine, J. S. Lintuvuori, J.-F. Boudet, J.-C. Baret, and H. Kellay, Boundaries control collective dynamics of inertial self-propelled robots, Physical review letters 120, 188002 (2018).

- [35] X. Yang, C. Ren, K. Cheng, and H. Zhang, Robust boundary flow in chiral active fluid, Physical Review E 101, 022603 (2020).
- [36] A. Dmitriev, A. Rozenblit, V. Porvatov, A. Molodtsova, E. Puhtina, O. Burmistrov, D. Filonov, A. Souslov, and N. Olekhno, Statistical correlations in active matter based on robotic swarms, in 2021 International Conference Engineering and Telecommunication (En&T) (IEEE, 2021) pp. 1–3.
- [37] L. Giomi, N. Hawley-Weld, and L. Mahadevan, Swarming, swirling and stasis in sequestered bristle-bots, Proceedings of the Royal Society A: Mathematical, Physical and Engineering Sciences 469, 20120637 (2013).
- [38] G. Wang, T. V. Phan, S. Li, M. Wombacher, J. Qu, Y. Peng, G. Chen, D. I. Goldman, S. A. Levin, R. H. Austin, et al., Emergent field-driven robot swarm states, Physical review letters 126, 108002 (2021).
- [39] M. Leyman, F. Ogemark, J. Wehr, and G. Volpe, Tuning phototactic robots with sensorial delays, Physical Review E 98, 052606 (2018).
- [40] F. Arvin, J. Espinosa, B. Bird, A. West, S. Watson, and B. Lennox, Mona: an affordable mobile robot for swarm robotic applications, in *UK-RAS Conference on 'Robotics and Autonomous Systems* (2017) pp. 49–52.
- [41] S. K. Malu and J. Majumdar, Kinematics, localization and control of differential drive mobile robot, Global Journal of Research In Engineering (2014).
- [42] J. R. Howse, R. A. Jones, A. J. Ryan, T. Gough, R. Vafabakhsh, and R. Golestanian, Self-motile colloidal particles: from directed propulsion to random walk, Physical review letters 99, 048102 (2007).
- [43] C. Bechinger, R. Di Leonardo, H. Löwen, C. Reichhardt, G. Volpe, and G. Volpe, Active particles in complex and

- crowded environments, Reviews of Modern Physics 88, 045006 (2016).
- [44] J. Tailleur and M. Cates, Statistical mechanics of interacting run-and-tumble bacteria, Physical review letters 100, 218103 (2008).
- [45] A. P. Solon, M. E. Cates, and J. Tailleur, Active brownian particles and run-and-tumble particles: A comparative study, The European Physical Journal Special Topics 224, 1231 (2015).
- [46] H. C. Berg and D. A. Brown, Chemotaxis in escherichia coli analysed by three-dimensional tracking, Nature 239, 500 (1972).
- [47] N. Kumar, R. K. Gupta, H. Soni, S. Ramaswamy, and A. Sood, Trapping and sorting active particles: Motilityinduced condensation and smectic defects, Physical Review E 99, 032605 (2019).
- [48] L. Angelani, Averaged run-and-tumble walks, Europhysics Letters 102, 20004 (2013).
- [49] V. Balakrishnan, Elements of nonequilibrium statistical mechanics, Vol. 3 (Springer, 2008).
- [50] V. Balakrishnan, On a simple derivation of master equations for diffusion processes driven by white noise and dichotomic markov noise, Pramana 40, 259 (1993).
- [51] I. Santra, U. Basu, and S. Sabhapandit, Run-and-tumble particles in two dimensions: Marginal position distributions, Physical Review E 101, 062120 (2020).
- [52] U. Basu, S. N. Majumdar, A. Rosso, and G. Schehr, Active brownian motion in two dimensions, Physical Review E 98, 062121 (2018).